Engineering battery corrosion films by tuning electrical double layer composition

Xintong Yuan[1], Dongfang Cheng[1], Bo Liu[1], Kaiyan Liang[1], Keyue Liang[1], Jiayi Yu[1], Matthew Mecklenburg[2], Philippe Sautet[1,2,3], Yuzhang Li[1,2,4*]

[1]Department of Chemical and Biomolecular Engineering, University of California, Los Angeles, California 90095, USA

[2]California NanoSystems Institute (CNSI), University of California, Los Angeles, California 90095, USA

[3]Department of Chemistry and Biochemistry, University of California, Los Angeles, California 90095, USA

[4]Lead contact

*Corresponding: yuzhangli@ucla.edu

SUMMARY

Battery performance is strongly influenced by the solid electrolyte interphase (SEI) that forms from electrolyte decomposition and remains a key target for engineering design. Whereas traditional approaches to tune the SEI have focused on electrolyte chemistry, we show that manipulating the electric field offers a novel approach. Here, we change the electrical double layer (EDL) composition by either applying or removing the local electric field, which directly controls SEI formation. Surprisingly, the solvent-derived SEI known to form in a conventional electrolyte exhibits anion-enhanced chemistry when the electric field is removed, which is attributed to the Coulombic interaction between the electric field and free anions. With the electric field control, we produce an anion-enhanced SEI in conventional electrolytes that demonstrates improved battery cycling and corrosion resistance. Together, our findings highlight the importance of EDL composition and demonstrate electric field strength as a new parameter to tune SEI structure and chemistry.

INTRODUCTION

Next-generation batteries with energy density beyond that of Li-ion largely depend on the Li metal anode, which is electrodeposited and stripped upon charging and discharging, respectively[1,2]. The reversibility of this electrodeposition process governs the performance of Li metal batteries but is complicated by electrolyte decomposition resulting in the formation of the solid electrolyte interphase (SEI)[3-5]. The SEI layer is ionically conductive yet electronically insulating, conformally passivating the Li metal surface from uncontrolled and continuous degradation[6,7]. The degree of passivation is believed to depend on the SEI chemistry, which is directly influenced by the components within the electrical double layer (EDL) that are decomposed to form the SEI[8-11]. For example, SEI chemistries derived from anion decomposition (i.e., anion-derived SEI) have been shown to enable much higher cycling efficiencies and Li electrodeposition reversibility than SEI chemistries derived from solvent decomposition (i.e., solvent-derived SEI)[12-16]. As a result, producing anion-derived SEI films has emerged as a key design principle in Li metal battery research. One of the approaches for forming anion-derived SEI films has been to engineer the solvation structure of Li ions to contain more anions by using weakly solvating solvents or ultrahigh concentration regimes[17-19]. This allows for anions within the solvation shell of Li ions to remain at the EDL interface for decomposition and incorporation into the SEI film. In contrast, the free, unsolvated anions in conventional electrolytes with solvent-dominated Li^+ solvation shells are mostly repelled from the Helmholtz layer by the negative potentials applied[20] during Li electrodeposition, resulting in SEI films that are predominantly solvent-derived (Fig. 1A). While tuning the solvation structure has led to improvements in Li metal battery performance, it remains an indirect approach to control the composition of the EDL, which is what truly governs the SEI chemistry. Introducing desired decomposing components into the EDL[20,21] would enable more direct control over the resulting SEI chemistry and overall battery performance.

In this work, we show that the EDL composition and resulting SEI can be directly tuned by modulating the electric field, resulting in different SEI chemistry and structure in *the same electrolyte system*. We modify the electric field by changing the polarization of the Li metal surface. For example, the anode surface is negatively polarized during galvanostatic electrodeposition of Li metal, establishing an electric field that facilitates electrochemical decomposition of electrolyte to form the SEI layer. In the presence of an electric field, we term this SEI layer an "*electrochemical SEI*" (Fig. 1A). In contrast, an electric field is absent when the Li metal surface is not polarized. Any SEI formed on a non-polarized, pristine Li metal surface is then due to chemical decomposition, and we term this the "*chemical SEI*" (Fig. 1A). In this study, we compare chemical and structural differences between chemical SEI (electric field absent) and electrochemical SEI (electric field present). 1M lithium hexafluorophosphate ($LiPF_6$) in 1:1 v/v ethylene carbonate (EC)/ diethyl carbonate (DEC) is an appropriate model system to study how the electric field can influence the EDL composition. In this electrolyte, the dipole-ion interactions between Li^+ and solvent result in reduced likelihood of salt anions being solvated by Li^+ such that the inner layer of the Li^+ solvation structure is dominated by EC, while PF_6^- ions are excluded[22,23]. Consequently, EC tends to decompose on the Li metal surface, forming a typical solvent-derived SEI that exhibits limited stability and mechanical properties, thus leading to a poor Coulombic efficiency (CE)[24,25]. Using 1M $LiPF_6$ in EC/DEC

as a model electrolyte system, we form electrochemical SEI (i.e., presence of an electric field) by conventional galvanostatic electrodeposition at a constant current density. In the same electrolyte, we form chemical SEI by immersing mechanically polished Li foil in liquid electrolyte. Equivalently, chemical SEI can also be formed using ultrafast Li electrodeposition, unique conditions under which SEI formation is decoupled from Li deposition. Our previous work[26] showed any SEI formed under such conditions is stepwise (i.e., chemically formed after initial Li metal nucleation).

Here, we discover that these electrochemical and chemical SEI films are distinct from one another due to either the presence or absence of an electric field changing the EDL composition. Specifically, we find that in the absence of an electric field, EDL components in a conventional electrolyte (i.e., 1M $LiPF_6$ in EC/DEC) decompose on the Li metal surface to form an anion-enhanced SEI film (i.e., chemical SEI). This is in stark contrast to the solvent-derived SEI film formed in the same electrolyte under an applied electric field during electrodeposition (i.e., electrochemical SEI). Beyond changes in SEI chemistry, our cryogenic-electron microscopy (cryo-EM)[27] experiments show that the chemical SEI film formed without an electric field is 50% thinner than the electrochemical SEI film formed with an electric field. We attribute these structural and chemical changes in the SEI to the compositional differences in the EDL when applying or removing an electric field (i.e., repulsion of the anion), which is supported by both grand canonical density functional theory (GCDFT) simulation and *in situ* electrochemical surface-enhanced Raman spectroscopy (SERS) measurements. The anion-enhanced, chemical SEI formed in the absence of an electric field provides improved chemical stability and passivation compared with its solvent-derived counterpart formed in the presence of an electric field. In the context of battery performance, this chemical stability manifests in the resilience to corrosion during 24 hour calendar aging[28,29] and reduced voltage hysteresis during battery cycling. These results introduce electric field as a complementary pathway towards controlling SEI structure and chemistry, with direct implications for battery performance. More broadly, our work encourages alternative approaches to tune the EDL composition (i.e., beyond electric field and solvation structure), which will further efforts in engineering optimal SEI films for future battery chemistries.

RESULTS

To reveal how the presence or absence of an electric field changes the overall chemistry of an SEI film formed in this model electrolyte, we use X-ray photoelectron spectroscopy (XPS), which can distinguish between different types of chemical bonding. Organic SEI components are typically correlated with stronger C 1s peaks, while inorganic SEI components contain more Li, O, and F signals from their respective 1s peaks (Fig. 1B). The ratio of Li, O, or F spectra peaks to that of C then quantifies the relative amounts of inorganic components in SEI films (Fig. 1C). In our model electrolyte system (i.e., 1M $LiPF_6$ in EC/DEC), XPS spectra show that the electrochemical SEI (formed under an electric field) contains mostly organic, solvent-derived components (Fig. 1B, C), which is consistent with previous works[30-32]. High resolution XPS scans (Fig. 1E) also show stronger signals in C-C (284.8 eV) and C-O (286.4 eV) bonding, which are strongly correlated with polymeric SEI components derived from the organic solvent[30,32]. In contrast, chemical SEI formed in the absence of an electric field in this same

model electrolyte demonstrates enhanced inorganic components (Fig. 1B, C). This is evidenced by the large increase (> 3-fold) in the ratio of F to C signals in the chemical SEI film, which persists throughout the thickness of the SEI film (Fig. 1D). High resolution XPS scans of the F and Li (Fig. 1E) show that chemical SEI contains increased LiF (56.3 eV), which is known to form from the decomposition of the PF_6^- anion[32]. Normally under an electric field, anion decomposition is disfavored in this strongly solvating electrolyte system. We show that by removing the electric field, more anions are decomposed and incorporated into the SEI as inorganic components.

In addition to changes in SEI chemistry, the electric field appears to also influence the local nanostructure of the SEI. Using cryo-EM (see methods), we find distinct differences in the (1) thickness, (2) nanostructure, and (3) chemistry of the chemical and electrochemical SEI. We determine the thickness of an SEI film by averaging ~50 cryo-EM imaging measurements taken from different regions across the deposited Li metal (Fig. 2A and F). Interestingly, our histogram of these SEI thicknesses (Fig. 2B and G) shows that the electrochemical SEI (~15 ± 2 nm) is 50% thicker than the chemical SEI (~10 ± 1 nm). This suggests that the inorganic components found in the chemical SEI are more electronically insulating, thus forming a thinner passivating SEI film than the electrochemical SEI that is more organic in nature. This passivating property of the chemical SEI has direct implications on improving battery performance (see below). Cryo-EM also reveals distinct nanostructures of chemical and electrochemical SEI films. During battery operating conditions with an applied electric field, the electrochemical SEI exhibits the classic *mosaic structure* (Fig. 2H, I and S1), which was originally proposed by Peled et al.[33] and directly imaged by Li et al.[34] using cryo-EM. The *mosaic structure* contains nanocrystalline domains (e.g., Li_2O, identified by matching lattice spacings) dispersed heterogeneously within an amorphous matrix. This distribution of nanocrystalline grains can dramatically impact the uniformity of Li-ion transport through the SEI[35]. In the absence of an electric field, the chemical SEI instead exhibits a *hybrid* nanostructure, a combination of the *mosaic* model and the *multilayer* model[34,36] in which the inorganic and organic domains are arranged in an ordered, multilayer fashion (Fig. 2C, D and S2). In addition to the structural motifs of the mosaic model (e.g., nanocrystalline domains in an amorphous matrix), the chemical SEI displays an ordered distribution of Li_2O near the outer surface of the SEI film, which is a clear signature of the multilayer SEI nanostructure. This ordered SEI nanostructure improves the uniformity of Li-ion transport through the SEI, mitigating inactive Li formation during the stripping process[35]. Finally, we chemically map the various SEI films using energy-dispersive spectroscopy (EDS) in scanning transmission electron microscopy (STEM) mode to reveal a stronger presence of O and F in the chemical SEI than electrochemical SEI (Fig. 2E, J and Table S1), which is consistent with our XPS results. Together, XPS and cryo-EM show that the chemical SEI formed in the absence of the electric field has a distinct chemistry and nanostructure, which is more inorganic and anion-enhanced in nature compared to its electrochemical SEI counterpart.

When SEI films form in the same electrolyte chemistry, the clear differences observed between chemical and electrochemical SEI are likely due to the absence or presence of an external electric field. While spontaneous redox reactions and charge transfer can form a localized

electric field, the range of this field is small and its intensity is negligible (an order of magnitude lower) compared to an externally applied electric field. We propose that the electric field strongly influences EDL composition, which will directly impact which components are reduced to form the SEI film. For example, free anions in our model electrolyte system are likely repelled from the EDL interface by the negatively polarized Li metal surface during electrodeposition (Fig. 1A), which would result in predominantly solvent-derived SEI films formed in the presence of an electric field. We use *in situ* electrochemical SERS to provide experimental evidence for this explanation. Peaks observed in Raman spectra correspond to vibrational modes of specific chemical bonds. By using SERS to measure how the peak signals corresponding to the PF_6^- anion and EC solvent molecule evolve, we can determine how the EDL composition changes as a function of electrode potential. The peak at 740 cm^{-1} corresponds to the stretching P-F bond in free PF_6^- anion (i.e., outside the solvation shell) when it is dissolved in the electrolyte solvent (Fig. S3A). The peak at 715 cm^{-1} corresponds to the bending O-C-O bond in the EC solvent molecule (Fig. S3A). The ratio between the intensities of these two peaks is then a quantitative descriptor for the relative amount of anion present (Fig. S3B). By adding Au nanoparticles[8,23] to our current collector, we can enhance the Raman signal originating from the surface EDL and track how the relative amounts of anion and solvent molecule change as we vary the electrode potential. As the electrode surface is negatively polarized, we expect the negatively charged anions to be repelled away from the EDL and the neutral EC molecule to be largely unaffected by this coulombic interaction (Fig. 3A). Indeed, this is precisely what our *in situ* electrochemical SERS experiment demonstrates: as the electrode potential decreases below zero, the ratio of the PF_6^-/EC peaks decreases by almost 20% (Fig. 3B). This results in less anions being present within the EDL for decomposition and incorporation into the SEI layer and explains the observed differences between chemical and electrochemical SEI.

In addition to *in situ* electrochemical analysis, GCDFT calculations are performed under a constant potential based on the loop-iteration method to support the observed phenomenon (see methods). We explore the distance, adsorption strength, and Li-F bond strength at the molecular scale as a function of potential to quantify the attraction and repulsion behaviors between PF_6^- and the Li surface. Our investigation reveals that the PF_6^- molecule chemisorbs to the Li surface through three robust F-Li bonds under positive potential, gradually transitioning to physisorption with increased separation and weakened bonds as the potential becomes negative (Fig. 3A, S4). A nearly-linear relationship is shown between the applied voltage and the distance between $PF_6^-$and the Li surface. In other words, increasing the negative polarization of the Li surface repels and separates PF_6^- from the Li metal (Fig. 3B). The relationship between the relative position of PF_6^- and the Li surface has been further elucidated through a detailed analysis of the Li-F bonds. With increasing negative potentials, there is a linear decrease in both the Integrated Crystal Orbital Hamilton Populations (ICOHP) and the bond order corresponding to the Li-F interactions, suggestive of a progressive weakening of these bonds (Fig. 3C). The cleavage of a single Li-F bond results in a pronounced decline in the cumulative bond strength. Notably, at a potential of -0.6 V vs Li^+/Li, the interaction between Li and F atoms diminishes to the point of nonexistence, indicative of a repulsive interaction. To illustrate, more positive potentials favor PF_6^- adsorption, while PF_6^- desorbs from the Li surface at more

negative potentials (Fig. 3A). While it is qualitatively expected that negative potentials would repel anions like PF_6^-, our calculations here provide a quantitative explanation for how the PF_6^- adsorption behavior is modulated by the applied potential and show how the transition between adsorbed and non-adsorbed anions occurs. The molecular-level changes observed through computational analysis align consistently with our experimental findings obtained from *in situ* SERS.

Our findings reveal that the presence or absence of an electric field can influence the composition of the EDL by Coulombic interactions with free anions, thus changing the structure and chemistry of the resulting SEI film. Since the electric field strength can vary dramatically across any electrode surface that is not atomically uniform[37,38], our results may explain the spatial non-uniformity observed in SEI films formed in electrolytes with many free anions. Specifically, the local concentration of anions within the EDL across the electrode surface may vary substantially due to changes in the local electric field[8,9], thus causing non-uniformity in the SEI structure and chemistry. For electrolyte chemistries that don't have as many free anions responding to the electric field (e.g., highly concentrated electrolytes), we would expect this spatial variation in electric field to have less of an impact on the resulting SEI film uniformity. In other words, there should not be much distinction between the chemical and electrochemical SEI formed in electrolytes with more anions in the solvation structure. Experimental observations of the chemical and electrochemical SEI films formed in a highly concentrated electrolyte support this conclusion. Due to increased viscosity and insolubility of concentrated $LiPF_6$ (less than 3M) in EC/DEC, we choose 4M Li bis(fluorosulfonyl)imide (LiFSI) in dimethoxyethane (DME)[39,40] as the representative of a highly concentrated electrolyte system with a Li^+ solvation structure containing a larger amount of anions (Fig. S5) than conventional electrolytes such as 1M $LiPF_6$ in EC/DEC. Because this electrolyte has fewer free anions that can respond to an electric field (Fig. S6), the chemical and electrochemical SEI formed in 4M LiFSI in DME is observed to be similar. Our cryo-EM images confirm that chemical and electrochemical SEI in 4M LiFSI in DME have similar thickness (~11 nm, Fig. 4A, B and E, F) and nanostructure with abundant dispersed Li_2O and LiF within an amorphous matrix (Fig. 4C, G and S7, S8). Furthermore, STEM EDS show that the distribution of O, F, C, S and N within the chemical and electrochemical SEI are similarly uniform (Fig. 4D and H). Whereas the F/C ratios of chemical and electrochemical SEI differ by more than a factor of three in 1M $LiPF_6$ in EC/DEC, the chemical and electrochemical SEI formed in 4M LiFSI in DME have similar F/C ratio (Table S2). As a result, the SEI films formed in 4M LiFSI are less susceptible to changes in electric field and thus have more uniform structure and composition, leading to enhanced battery performance[39].

When formed in the absence of an electric field, the chemical SEI is found to be rich in anion components even in conventional electrolytes like 1M $LiPF_6$ in EC/DEC, which is normally solvent-derived. This has important implications for battery performance since anion-enhanced SEI chemistries are typically associated with strong passivating properties that prevent continued SEI growth. To demonstrate the enhancement that chemical SEI provides for battery cycling and calendar aging, we build Li||lithium iron phosphate (LFP) cells using (1) pristine Li foil and (2) Li foil immersed in liquid electrolyte for 24 hours to form a more developed

chemical SEI (Fig. S9). With the chemical SEI, Li||LFP cells exhibit much lower voltage hysteresis between charging and discharging voltage plateaus (~100 mV, Fig. 5A and B) than cells without chemical SEI (~250 mV, Fig. 5C and D). This suggests that the chemical SEI has high ionic conductivity and does not contribute excess impedance compared to even pristine Li foil. Thus, we observe higher capacity and CE for the chemical SEI coin cells in the early cycles, minimizing excess SEI formation (Fig. 5E). Furthermore, we show that the capacity loss due to 24-hour calendar aging is substantially reduced in chemical SEI coin cells, with less than half as much loss compared with coin cells without chemical SEI (Fig. 5F). Our cryo-EM experiments show that the chemical SEI is much more passivating during calendar aging, with the SEI thickness increasing slightly (~5 nm) during 24-hour rest at open circuit voltage (Fig. 5G, H and S10A). In contrast, the electrochemical SEI does not offer as much passivation, growing nearly 40 to 80 nm non-uniformly across the Li dendrite after 24-hour calendar aging (Fig. 5I, J and S10B).

In addition to resting and growing chemical SEI before battery cycling, we also suggest periodically adding a rest period where the electric field is removed, allowing anion enrichment in the EDL for chemical SEI formation (anion-enhanced). We use a pulse-current deposition approach in the electrolyte of 1M $LiPF_6$ in EC/DEC at a current density of 1 mA cm^{-2}, with repeated deposition for 1 s and resting for 3 s, until a capacity of 1 mAh cm^{-2} is reached. Subsequently, the stripping current density is 1 mA cm^{-2} with a cut off voltage of 1V. As a control experiment, standard galvanostatic cycling (i.e., no rest period) is performed at a constant current density of 1 mA cm^{-2} for the same capacity. The SEI formed during pulse-current deposition (i.e., "pulse SEI") exhibits the properties intermediate between chemical SEI and electrochemical SEI, including SEI thickness (e.g., pulse SEI thickness is around 13 nm in Fig. 6A and B, compared to 10 nm for chemical SEI and 15 nm for electrochemical SEI), chemical components (e.g., pulse SEI contains LiF in Fig. 6C, while chemical SEI contains LiF and electrochemical SEI has no LiF particles in cryo-EM images), and elemental ratios (F/C ratio in pulse SEI is around 0.15, compared to around 0.3 in chemical SEI and around 0.1 in electrochemical SEI, Fig. 6D, E and Table S1). The formation of pulse SEI facilitates a more uniform and dense Li growth (Fig. S11), leading to increased reversibility of Li stripping. Thus, we observe a 4% CE increase (Fig. 6F) for the pulse-current protocol in the Li-Cu coin cell geometry. These results show that the passivating properties of the chemical SEI can positively impact battery performance and motivate the future design of optimal protocols leveraging the electric field to form more ideal SEI films.

DISCUSSION

Our work reveals that the SEI structure and chemistry is strongly influenced by the EDL composition, which can be tuned by the electric field. At negative surface potentials forming an electric field, we show that the electrochemical SEI exhibits solvent-derived components. Without the electric field present, the chemical SEI is more anion rich due to a larger concentration of free anions within the EDL. The impact of the electric field on the EDL composition is shown experimentally using *in situ* electrochemical Raman and theoretically using GCDFT. These findings lead to new insights for battery research: (1) that spatial variation in the electric field will lead to SEI non-uniformity and (2) that SEI films normally exhibiting

solvent-derived compositions can be engineered to anion-enhanced chemistries to improve battery cycling and corrosion resistance. More broadly, our results will encourage future approaches to tune the EDL composition that can enable closer control over SEI structure and composition.

EXPERIMENTAL PROCEDURES

Resource availability

Lead contact

Further information and requests for resources and materials should be directed to and will be fulfilled by the lead contact, Yuzhang Li (yuzhangli@ucla.edu).

Materials availability

This study did not generate new unique materials.

Data and code availability

All data needed to evaluate the conclusions in this paper are present in the paper or the supplemental information. This study did not generate code.

Preparation of electrolyte solutions

Lithium hexafluorophosphate solution in ethylene carbonate and diethyl carbonate (1 M $LiPF_6$ in EC/DEC) was directly purchased from Sigma-Aldrich with battery grade. Lithium bis(fluorosulfonyl)imide (LiFSI, Canrd, 99.5%) were dried at 65 ^{o}C overnight prior to using. dimethoxyethane (DME, Sigma-Aldrich, 99.5%) was added to obtain 4 M solution of LiFSI (4M LiFSI in DME). All chemicals were used as received without further purification. All electrolytes were made and stored in the Ar-filled glovebox (O_2 < 0.2 ppm, H_2O < 0.02 ppm).

Electrochemical experiments

In Li||LFP 2032-type coin cells, LFP foil (mass percent of active material is around 88%, area mass loading of active material on current collector is around 12 mg cm^{-2}, Canrd) of 10 mm in diameter was served as working electrode and Li foil (70 μm thick, Canrd) of 15 mm in diameter was served as the counter/ reference electrode. Li foil was mechanically sheared using a polyethylene scraper to remove the surface oxide and improve electrical connection to the stainless-steel coin cell case. After mechanically shearing, the clean pristine Li foil was used to make coin cells with below procedures is the blank control sample. Li foil along with a chemical SEI was obtained by immersing Li foil in 1M $LiPF_6$ in EC/DEC for 24 hours.

In Li||Cu 2032-type coin cells, Cu foil (10 μm thick, Canrd, 99%) of 12 mm in diameter served as the working electrode, while Li foil of 10 mm in diameter served as the counter/reference electrode. Similar with Li||LFP cell, Li foil was mechanically sheared for processing prior using. Cu foil was rinsed with ultrapure water and acetone to remove surface contaminants before transferring into the glove box.

60 μL electrolyte was added to each cell using a 25 μm thick polypropylene-polyethylene-polypropylene separator (Celgard 2325) to divide the two electrodes. Coin cells were loaded onto a battery tester (Land Instruments) and cycled.

All battery assembly experiments were performed in the Ar-filled glovebox.

XPS sample preparation and characterization

XPS sample of electrochemical SEI were obtained by running Li||Cu 2032-type coin cells, a 300-mesh bare Cu TEM grid (TED PELLA) is incorporated onto Cu foil served as the working electrodes. Electrochemical SEI together with metallic Li were deposited on the TEM grid at a normal current density of 1 mA cm^{-2} for 10 min. During this process, the SEI grows concurrently with Li dendrites, indicating that this SEI is formed through the electrolyte decomposition under the influence of an electric field. After disassembling the coin cell in an Ar-filled glovebox, TEM grid was carefully raised with a few drops of anhydrous dioxolane. For the pulse SEI sample, the battery assembly was the same as that for the electrochemical SEI sample. The only difference is the addition of a 3 s pause for every 1 s of applying a current density of 1 mA cm^{-2}, with the total operation time maintained at 10 min. For the chemical SEI sample, after Li foil of 3 mm in diameter was mechanically sheared, it was immersed in 1M $LiPF_6$ in EC/DEC for 10 min to grow chemical SEI and carefully raised with a few drops of anhydrous dioxolane. Once dry, SEI samples were placed onto the XPS stage and then transferred to the XPS (Kratos AXIS Ultra DLD spectrometer) chamber using an air-tight transfer holder.

Cryo-EM sample preparation and imaging

Cryo-EM samples were obtained from Li||Cu coin cells. Their assembly was the same as Li||LFP cells, except that Cu foil of 12 mm diameter stacked together with a customized TEM grid served as the working electrodes. To grow chemical SEI on Li particles for convenient imaging through cryo-EM, we apply an ultrafast current density of 200 mA cm^{-2} to deposit faceted Li particles, effectively outpacing the SEI formation[26,41]. Subsequently, when the current ceased and the electric field is absent, chemical SEI is formed on the surface of the faceted Li particle due to physical contact with the electrolyte. To realize ultrafast current density, we used Cu chunk-based TEM grids as local ultramicroelectrodes prepared in the same way as our previous publication[26]. For a fair comparison, the combined duration of electrodeposition and standing time is 10 min for chemical SEI, consistent with the preparation time for the electrochemical SEI samples. The preparation process of electrochemical SEI and pulse SEI in cryo-EM is identical to that of the XPS sample described above.

After assembling the coin cell in an Ar-filled glovebox, TEM grid was carefully rinsed with a few drops of anhydrous dioxolane. Once dry, the TEM grid with deposited Li was placed in an Eppendorf tube sealed with parafilm and transferred out of glovebox. The pressure in the glovebox, and thus the sealed tube, was greater than ambient pressure, which prevented air from leaking into the tube. Outside the glovebox, pincer pliers held the sealed Eppendorf tube and plunged quickly into a bath of liquid nitrogen, then quickly crushed open the tube after 3 s while still immersed in the liquid nitrogen to expose the grid with deposited Li to cryogen immediately. The grid was stored in a cryo-grid box in liquid nitrogen dewar for usage.

To proceed with cryo-EM imaging, the TEM grid was mounted onto a Gatan 626 TEM cryo-transfer holder using a cryo-transfer station to make sure the whole process took place under liquid nitrogen. The built-in shutter on the transfer holder was kept closed to prevent air exposure and ice condensation onto the sample when inserting the holder into the TEM column. A liquid nitrogen dewar attached to the holder maintained the grid at cryogenic temperature

during the whole imaging process. All cryo-EM characterizations were carried out using an FEI Titan 80-300 scanning transmission electron microscope operated at 300 kV with a Gatan Ultrascan camera. During cryo-EM images acquisition, the corresponding electron dose flux was also recorded. Electron dose rate (flux) is less than 100 e $Å^{-2}$ s^{-1} for low magnification cryo-EM images and less than 1000 e $Å^{-2}$ s^{-1} for high resolution cryo-EM images. The electron beam exposure time of each image is no more than 30 s and the acquisition time is 0.4 to 1 s.

***In situ* surface enhanced Raman experiments**

A sealed three electrode electrochemical Raman cell (Gaoss Union) was used to perform *in situ* surface enhanced Raman experiments. A layer of coarse Au nanoparticles with a thickness of 20 nm was evaporated on the Cu mesh to serve as the working electrode for a surface enhancement effect and Li foil served as the counter/ reference electrode. The electrochemical potentiostat (BioLogic VMP3) was used to apply voltage on the Raman cell from OCV to -1 V vs Li^+/Li, and Raman scanning was carried out in the meantime. The Raman system (Renishaw) used in this experiment was equipped with a 785 nm diode laser.

GCDFT calculations

DFT calculations are performed using the Vienna Ab-Initio Simulation Package (VASP) with the PBE functional[42] and van der Waals interaction between atoms is corrected by using D3[43]. The core electrons are described with the projector augmented wave (PAW) method[44]. The convergence criteria for electronic and force minimization are set to 10^{-6} eV and 0.02 eV/Å for structure optimization. The cutoff energy for the kinetic energy of the plane-wave is 450 eV. (4 × 4)- 4 layer (110) surface is chosen for modelling Li, where the Brillouin zone is sampled using the (4 × 4 × 1) Gamma-centered k-point grid.

GCDFT are performed to obtain the potential-dependent energetics, where the number of electrons is allowed to change to adapt the change of work function along the reaction pathway. The potential-dependent grand canonical free energy can be expressed by a surface charging model:

$$\Omega(U) = \Omega(U) - q(U) \cdot FU \; = \; \Omega(U_0) - \frac{1}{2} C (U - U_0)^2$$

where $\Omega(U)$ is the electronic energy of the surface at the U potential in Standard Hydrogen Electrode (SHE) scale, $q(U)$ is the charge difference against the neutral condition, F is the Faradaic constant. C stands for the effective capacitance and U_0 represents the potential of zero charge (pzc). For more details of GCDFT, see our previous work[45-47]. The self-consistent implicit solvation model VASPsol is used to represent the polarizable electrolyte region. The dielectric constant 45.9, and the Debye screening length 2.33 Å, are used, as they correspond to the experimental electrolyte. We use a cutoff charge of 0.0002 to avoid unphysical invasion of the implicit solvent invasion into the Li layers[48]. The COHP analysis was performed using the LOBSTER program with the pbeVaspFit2015 basis set[49].

An iterative method is used to achieve structural optimization under constant potential rather than constant charge.

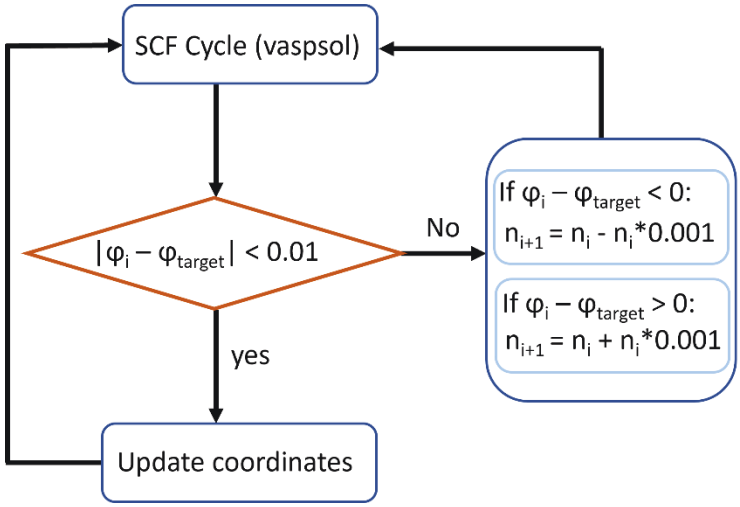

SUPPLEMENTAL INFORMATION

Supplemental information can be found online at

ACKNOWLEDGEMENTS

We acknowledge the support by the U.S. Department of Energy, Office of Science, Office of Basic Energy Sciences, under Award Number DE-SC0022955. We acknowledge the use of the UCLA-CNSI EICN Facilities and the support by the BioPACIFIC Materials Innovation Platform of the National Science Foundation under Award No. DMR-1933487. We thank Dr. Ankun Yang at Oakland University for his assistance with the Raman cell and experiment design. D.C. and P.S. acknowledge the National Science Foundation CBET grant 2103116, the Audi Cy Pres fund award, and computational resources from the Hoffman2 cluster at UCLA Institute for Digital Research and Education (IDRE) and the Expanse cluster through the allocation CHE170060 at the San Diego Supercomputing Center through ACCESS.

AUTHOR CONTRIBUTIONS

X.Y. and Y.L. conceived the project and designed the experiments. X.Y. performed electrochemical experiments, XPS, cryo-EM and *in situ* Raman characterizations. D.C. and P.S. helped with GCDFT simulations and data analysis. B.L. helped with electrochemical experiments and data analysis. Ka.L., Ke.L. and J.Y. were involved in general discussions. Ke.L. helped with partial cryo-EM samples preparation. M.M. advised on microscope and imaging analysis. X.Y. and Y.L. co-wrote the manuscript. All authors discussed the results and commented on the manuscript.

DECLARATION OF INTERESTS

The authors declare that they have no competing interests.

REFERENCES

1 Liu, B., Zhang, J.-G. and Xu, W. (2018). Advancing Lithium Metal Batteries. *Joule* **2**, 833-845. https://doi.org/10.1016/j.joule.2018.03.008.

2 Liu, B., Zhang, Y., Pan, G., Ai, C., Deng, S., Liu, S., Liu, Q., Wang, X., Xia, X. and Tu,

J. (2019). Ordered lithiophilic sites to regulate Li plating/stripping behavior for superior lithium metal anodes. *J. Mater. Chem. A* **7**, 21794-21801. https://doi.org/10.1039/c9ta09502k.

3 Lin, D., Liu, Y. and Cui, Y. (2017). Reviving the lithium metal anode for high-energy batteries. *Nat. Nanotechnol.* **12**, 194-206. https://doi.org/10.1038/nnano.2017.16.

4 Wu, H., Jia, H., Wang, C., Zhang, J. G. and Xu, W. (2020). Recent Progress in Understanding Solid Electrolyte Interphase on Lithium Metal Anodes. *Adv. Energy Mater.* **11**, 2003092. https://doi.org/10.1002/aenm.202003092.

5 Liu, B., Zhang, Y., Wang, Z., Ai, C., Liu, S., Liu, P., Zhong, Y., Lin, S., Deng, S., Liu, Q. *et al.* (2020). Coupling a Sponge Metal Fibers Skeleton with In Situ Surface Engineering to Achieve Advanced Electrodes for Flexible Lithium-Sulfur Batteries. *Adv. Mater.* **32**, e2003657. https://doi.org/10.1002/adma.202003657.

6 Zhao, Q., Stalin, S. and Archer, L. A. (2021). Stabilizing metal battery anodes through the design of solid electrolyte interphases. *Joule* **5**, 1119-1142. https://doi.org/10.1016/j.joule.2021.03.024.

7 Xu, Y., Jia, H., Gao, P., Galvez-Aranda, D. E., Beltran, S. P., Cao, X., Le, P. M. L., Liu, J., Engelhard, M. H., Li, S. *et al.* (2023). Direct in situ measurements of electrical properties of solid–electrolyte interphase on lithium metal anodes. *Nat. Energy* **8**, 1345–1354. https://doi.org/10.1038/s41560-023-01361-1.

8 Zhang, W., Lu, Y., Wan, L., Zhou, P., Xia, Y., Yan, S., Chen, X., Zhou, H., Dong, H. and Liu, K. (2022). Engineering a passivating electric double layer for high performance lithium metal batteries. *Nat. Commun.* **13**, 2029. https://doi.org/10.1038/s41467-022-29761-z.

9 Yan, C., Li, H. R., Chen, X., Zhang, X. Q., Cheng, X. B., Xu, R., Huang, J. Q. and Zhang, Q. (2019). Regulating the Inner Helmholtz Plane for Stable Solid Electrolyte Interphase on Lithium Metal Anodes. *J. Am. Chem. Soc.* **141**, 9422-9429. https://doi.org/10.1021/jacs.9b05029.

10 Xu, R., Shen, X., Ma, X. X., Yan, C., Zhang, X. Q., Chen, X., Ding, J. F. and Huang, J. Q. (2021). Identifying the Critical Anion-Cation Coordination to Regulate the Electric Double Layer for an Efficient Lithium-Metal Anode Interface. *Angew. Chem. Int. Ed.* **60**, 4215-4220. https://doi.org/10.1002/anie.202013271.

11 Wu, Q., McDowell, M. T. and Qi, Y. (2023). Effect of the Electric Double Layer (EDL) in Multicomponent Electrolyte Reduction and Solid Electrolyte Interphase (SEI) Formation in Lithium Batteries. *J. Am. Chem. Soc.* **145**, 2473-2484. https://doi.org/10.1021/jacs.2c11807.

12 Wang, H., Yu, Z., Kong, X., Kim, S. C., Boyle, D. T., Qin, J., Bao, Z. and Cui, Y. (2022). Liquid electrolyte: The nexus of practical lithium metal batteries. *Joule* **6**, 588-616. https://doi.org/10.1016/j.joule.2021.12.018.

13 Ren, X., Gao, P., Zou, L., Jiao, S., Cao, X., Zhang, X., Jia, H., Engelhard, M. H., Matthews, B. E., Wu, H. *et al.* (2020). Role of inner solvation sheath within salt-solvent complexes in tailoring electrode/electrolyte interphases for lithium metal batteries. *Proc. Natl. Acad. Sci. U. S. A.* **117**, 28603-28613. https://doi.org/10.1073/pnas.2010852117.

14 Yu, Z., Rudnicki, P. E., Zhang, Z., Huang, Z., Celik, H., Oyakhire, S. T., Chen, Y., Kong,

X., Kim, S. C., Xiao, X. *et al.* (2022). Rational solvent molecule tuning for high-performance lithium metal battery electrolytes. *Nat. Energy* **7**, 94-106. https://doi.org/10.1038/s41560-021-00962-y.

15 Xu, K. (2014). Electrolytes and interphases in Li-ion batteries and beyond. *Chem. Rev.* **114**, 11503-11618. https://doi.org/10.1021/cr500003w.

16 Chen, J., Fan, X., Li, Q., Yang, H., Khoshi, M. R., Xu, Y., Hwang, S., Chen, L., Ji, X., Yang, C. *et al.* (2020). Electrolyte design for LiF-rich solid–electrolyte interfaces to enable high-performance microsized alloy anodes for batteries. *Nat. Energy* **5**, 386-397. https://doi.org/10.1038/s41560-020-0601-1.

17 Wang, H., Huang, W., Yu, Z., Huang, W., Xu, R., Zhang, Z., Bao, Z. and Cui, Y. (2021). Efficient Lithium Metal Cycling over a Wide Range of Pressures from an Anion-Derived Solid-Electrolyte Interphase Framework. *ACS Energy Lett.* **6**, 816-825. https://doi.org/10.1021/acsenergylett.0c02533.

18 Ren, X., Chen, S., Lee, H., Mei, D., Engelhard, M. H., Burton, S. D., Zhao, W., Zheng, J., Li, Q., Ding, M. S. *et al.* (2018). Localized High-Concentration Sulfone Electrolytes for High-Efficiency Lithium-Metal Batteries. *Chem* **4**, 1877-1892. https://doi.org/10.1016/j.chempr.2018.05.002.

19 Cao, X., Gao, P., Ren, X., Zou, L., Engelhard, M. H., Matthews, B. E., Hu, J., Niu, C., Liu, D., Arey, B. W. *et al.* (2021). Effects of fluorinated solvents on electrolyte solvation structures and electrode/electrolyte interphases for lithium metal batteries. *Proc. Natl. Acad. Sci. U. S. A.* **118**, e2020357118 https://doi.org/10.1073/pnas.2020357118.

20 Jiang, L., Li, D., Xie, X., Ji, D., Li, L., Li, L., He, Z., Lu, B., Liang, S. and Zhou, J. (2023). Electric double layer design for Zn-based batteries. *Energy Storage Mater.* **62**, 102932. https://doi.org/10.1016/j.ensm.2023.102932.

21 Li, D., Tang, Y., Liang, S., Lu, B., Chen, G. and Zhou, J. (2023). Self-assembled multilayers direct a buffer interphase for long-life aqueous zinc-ion batteries. *Energy Environ. Sci.* **16**, 3381-3390. https://doi.org/10.1039/d3ee01098h.

22 Daniel M. Seo, Joshua Lee Allen, Lindsay A. Gardner, Sang-Don Han, Boyle, P. D. and Henderson, W. A. (2013). Electrolyte Solvation and Ionic Association: Cyclic Carbonate and Ester-LiTFSI and -LiPF6 Mixtures. *ECS Trans.* **50**, 375-380.

23 Yang, G., Ivanov, I. N., Ruther, R. E., Sacci, R. L., Subjakova, V., Hallinan, D. T. and Nanda, J. (2018). Electrolyte Solvation Structure at Solid-Liquid Interface Probed by Nanogap Surface-Enhanced Raman Spectroscopy. *ACS Nano* **12**, 10159-10170. https://doi.org/10.1021/acsnano.8b05038.

24 Han, B., Zhang, Z., Zou, Y., Xu, K., Xu, G., Wang, H., Meng, H., Deng, Y., Li, J. and Gu, M. (2021). Poor Stability of Li(2) CO(3) in the Solid Electrolyte Interphase of a Lithium-Metal Anode Revealed by Cryo-Electron Microscopy. *Adv. Mater.* **33**, e2100404. https://doi.org/10.1002/adma.202100404.

25 Gao, Y., Du, X., Hou, Z., Shen, X., Mai, Y.-W., Tarascon, J.-M. and Zhang, B. (2021). Unraveling the mechanical origin of stable solid electrolyte interphase. *Joule* **5**, 1860-1872. https://doi.org/10.1016/j.joule.2021.05.015.

26 Yuan, X., Liu, B., Mecklenburg, M. and Li, Y. (2023). Ultrafast deposition of faceted lithium polyhedra by outpacing SEI formation. *Nature* **620**, 86-91. https://doi.org/10.1038/s41586-023-06235-w.

27 Zhang, E., Mecklenburg, M., Yuan, X., Wang, C., Liu, B. and Li, Y. (2022). Expanding the cryogenic electron microscopy toolbox to reveal diverse classes of battery solid electrolyte interphase. *iScience* **25**, 105689. https://doi.org/10.1016/j.isci.2022.105689.

28 Liu, B., Yuan, X. and Li, Y. (2023). Colossal Capacity Loss during Calendar Aging of Zn Battery Chemistries. *ACS Energy Lett.* **8**, 3820-3828. https://doi.org/10.1021/acsenergylett.3c01282.

29 Boyle, D. T., Huang, W., Wang, H., Li, Y., Chen, H., Yu, Z., Zhang, W., Bao, Z. and Cui, Y. (2021). Corrosion of lithium metal anodes during calendar ageing and its microscopic origins. *Nat. Energy* **6**, 487–494. https://doi.org/10.1038/s41560-021-00787-9.

30 Zhao, Y., Zhou, T., Jeurgens, L. P. H., Kong, X., Choi, J. W. and Coskun, A. (2023). Electrolyte engineering for highly inorganic solid electrolyte interphase in high-performance lithium metal batteries. *Chem* **9**, 547-549. https://doi.org/10.1016/j.chempr.2022.12.005.

31 Tan, Y. H., Lu, G. X., Zheng, J. H., Zhou, F., Chen, M., Ma, T., Lu, L. L., Song, Y. H., Guan, Y., Wang, J. *et al.* (2021). Lithium Fluoride in Electrolyte for Stable and Safe Lithium-Metal Batteries. *Adv. Mater.* **33**, e2102134. https://doi.org/10.1002/adma.202102134.

32 Guo, R., Wang, D., Zuin, L. and Gallant, B. M. (2021). Reactivity and Evolution of Ionic Phases in the Lithium Solid–Electrolyte Interphase. *ACS Energy Lett.* **6**, 877-885. https://doi.org/10.1021/acsenergylett.1c00117.

33 E. Peled, D. G. a. G. A. (1997). Advanced Model for Solid Electrolyte Interphase Electrodes in Liquid and Polymer Electrolytes. *J. Electrochem. Soc.* **144**, L208

34 Li, Y., Li, Y., Pei, A., Yan, K., Sun, Y., Wu, C.-L., Joubert, L.-M., Chin, R., Koh, A. L., Yu, Y. *et al.* (2017). Atomic structure of sensitive battery materials and interfaces revealed by cryo–electron microscopy. *Science* **358**, 506-510.

35 Li, Y., Huang, W., Li, Y., Pei, A., Boyle, D. T. and Cui, Y. (2018). Correlating Structure and Function of Battery Interphases at Atomic Resolution Using Cryoelectron Microscopy. *Joule* **2**, 2167-2177. https://doi.org/10.1016/j.joule.2018.08.004.

36 Doron Aurbach, Yair Ein- Ely and Zaban, A. (1994). The Surface Chemistry of Lithium Electrodes in Alkyl Carbonate Solutions. *J. Electrochem. Soc.* **141**, L1.

37 Zhang, X., Wang, A., Liu, X. and Luo, J. (2019). Dendrites in Lithium Metal Anodes: Suppression, Regulation, and Elimination. *Acc. Chem. Res.* **52**, 3223-3232. https://doi.org/10.1021/acs.accounts.9b00437.

38 Liu, M., Pang, Y., Zhang, B., De Luna, P., Voznyy, O., Xu, J., Zheng, X., Dinh, C. T., Fan, F., Cao, C. *et al.* (2016). Enhanced electrocatalytic CO2 reduction via field-induced reagent concentration. *Nature* **537**, 382-386. https://doi.org/10.1038/nature19060.

39 Qian, J., Henderson, W. A., Xu, W., Bhattacharya, P., Engelhard, M., Borodin, O. and Zhang, J. G. (2015). High rate and stable cycling of lithium metal anode. *Nat. Commun.* **6**, 6362. https://doi.org/10.1038/ncomms7362.

40 Holoubek, J., Liu, H., Wu, Z., Yin, Y., Xing, X., Cai, G., Yu, S., Zhou, H., Pascal, T. A., Chen, Z. *et al.* (2021). Tailoring Electrolyte Solvation for Li Metal Batteries Cycled at Ultra-Low Temperature. *Nat. Energy* **6**, 303-313. https://doi.org/10.1038/s41560-021-

00783-z.
41 Boyle, D. T., Kong, X., Pei, A., Rudnicki, P. E., Shi, F., Huang, W., Bao, Z., Qin, J. and Cui, Y. (2020). Transient Voltammetry with Ultramicroelectrodes Reveals the Electron Transfer Kinetics of Lithium Metal Anodes. *ACS Energy Lett.* **5**, 701-709. https://doi.org/10.1021/acsenergylett.0c00031.
42 G. Kresse and Furthmüller, J. (1996). Efficient iterative schemes for ab initio total-energy calculations using a plane-wave basis set. *Phys. Rev. B* **54**, 11169.
43 Grimme, S., Antony, J., Ehrlich, S. and Krieg, H. (2010). A consistent and accurate ab initio parametrization of density functional dispersion correction (DFT-D) for the 94 elements H-Pu. *J. Chem. Phys.* **132**, 154104. https://doi.org/10.1063/1.3382344.
44 G. Kresse and Joubert, D. (1999). From ultrasoft pseudopotentials to the projector augmented-wave method. *Phys. Rev. B* **59**, 1758.
45 Steinmann, S. N., Michel, C., Schwiedernoch, R. and Sautet, P. (2015). Impacts of electrode potentials and solvents on the electroreduction of CO2: a comparison of theoretical approaches. *Phys. Chem. Chem. Phys.* **17**, 13949-13963. https://doi.org/10.1039/c5cp00946d.
46 Steinmann, S. N. and Sautet, P. (2016). Assessing a First-Principles Model of an Electrochemical Interface by Comparison with Experiment. *J. Phys. Chem. C* **120**, 5619-5623. https://doi.org/10.1021/acs.jpcc.6b01938.
47 Steinmann, S. N., Sautet, P. and Michel, C. (2016). Solvation free energies for periodic surfaces: comparison of implicit and explicit solvation models. *Phys. Chem. Chem. Phys.* **18**, 31850-31861. https://doi.org/10.1039/c6cp04094b.
48 Peng, L., Wei, Z., Wan, C., Li, J., Chen, Z., Zhu, D., Baumann, D., Liu, H., Allen, C. S., Xu, X. *et al.* (2020). A fundamental look at electrocatalytic sulfur reduction reaction. *Nat. Catal.* **3**, 762-770. https://doi.org/10.1038/s41929-020-0498-x.
49 Nelson, R., Ertural, C., George, J., Deringer, V. L., Hautier, G. and Dronskowski, R. (2020). LOBSTER: Local orbital projections, atomic charges, and chemical-bonding analysis from projector-augmented-wave-based density-functional theory. *J. Comput. Chem.* **41**, 1931-1940. https://doi.org/10.1002/jcc.26353.

MAIN FIGURE LEGENDS

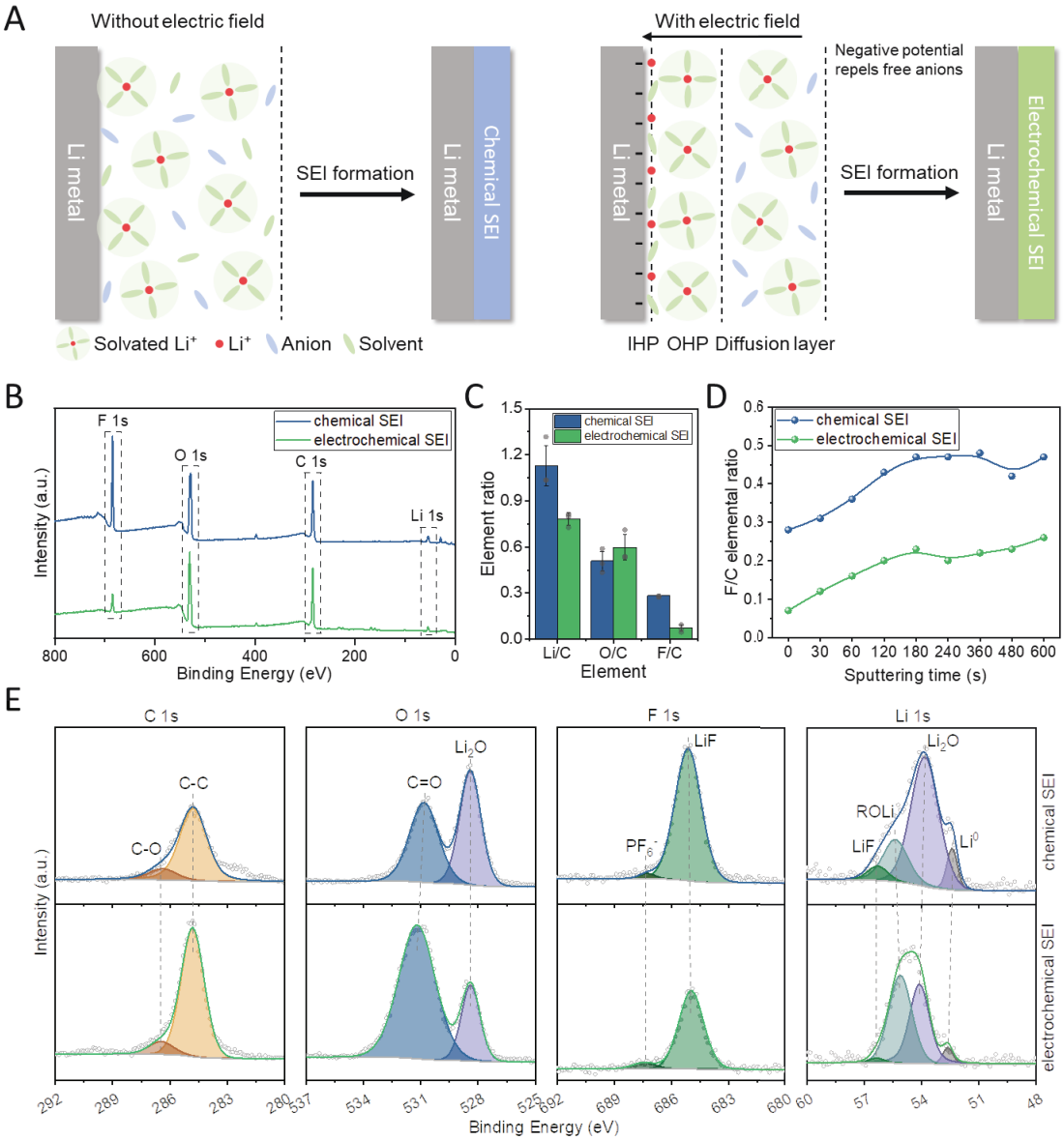

Fig. 1. Scheme and XPS analysis on chemical and electrochemical SEI showing that chemical SEI comprises more inorganic components in 1M $LiPF_6$ in EC/DEC. A) Scheme of chemical and electrochemical SEI formation processes. In the absence of an electric field, solvated Li^+, free anions and solvents are stochastic distributed (left). With applied electric field, inner Helmholtz plane (IHP) consists of desolvated Li^+ and solvents, while outer Helmholtz plane (OHP) is occupied by Li solvation structures, with free anions being repelled from the Helmholtz layer. B) XPS survey. C) The elemental ratios in the SEI calculated from (B). D) The elemental ratio of F/C obtained in the XPS depth profiles. E) High-resolution XPS spectra and fittings of C 1s, O 1s, F 1s and Li 1s.

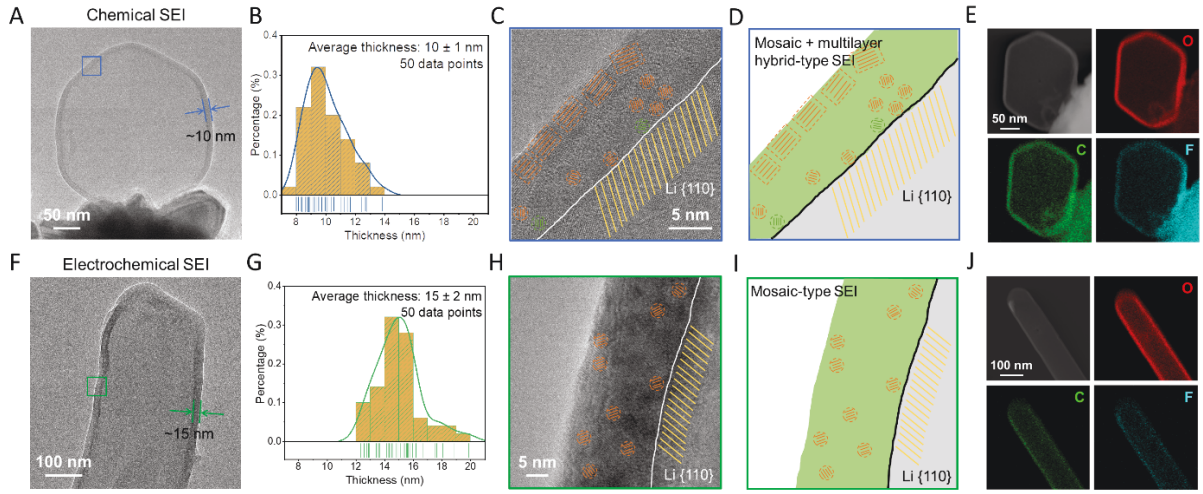

Fig. 2. Cryo-EM analysis on structure and chemistry of chemical and electrochemical SEI in 1M $LiPF_6$ in EC/DEC. A) Cryo-EM image of faceted Li particle covered with a layer of chemical SEI. B) Thickness statistics of chemical SEI. C) High-resolution cryo-EM image of chemical SEI layer, magnified from the blue box in (A). D) Schematic of observed mosaic plus multilayer hybrid type structure of chemical SEI in (C). E) STEM EDS mapping of chemical SEI. F-J) Analogous images to (A-E) but collected on electrochemical SEI.

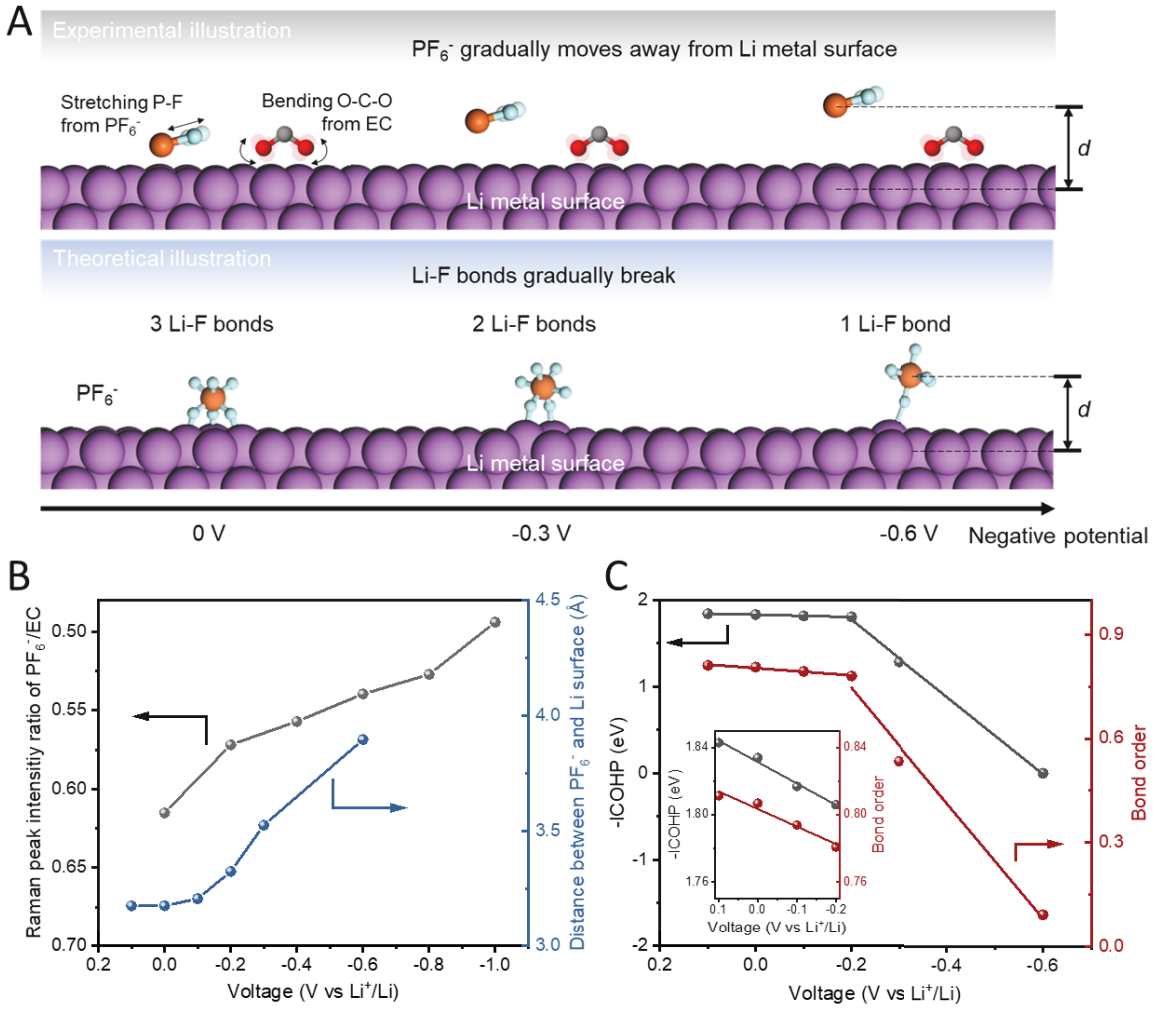

Fig. 3. Experimental and theoretical analysis showing anion's decay with negative voltage in 1M $LiPF_6$ in EC/DEC. A) Experimental illustration (top) showing stretching P-F from PF_6^- decays with the negative potential from *in situ* Raman spectra and theoretical illustration (bottom) of the interaction between PF_6^- and the Li surface as a function of the potential vs Li^+/Li. B) The variation trend of the absolute peak intensity of PF_6^- over EC (left) with respect to voltage calculated from *in situ* SERS and the distance between PF_6^- and Li surface (right) with respect to voltages from theoretical calculation. C) The cumulative ICOHP (left) and bond order (right) of Li-F bonds as the function of voltage.

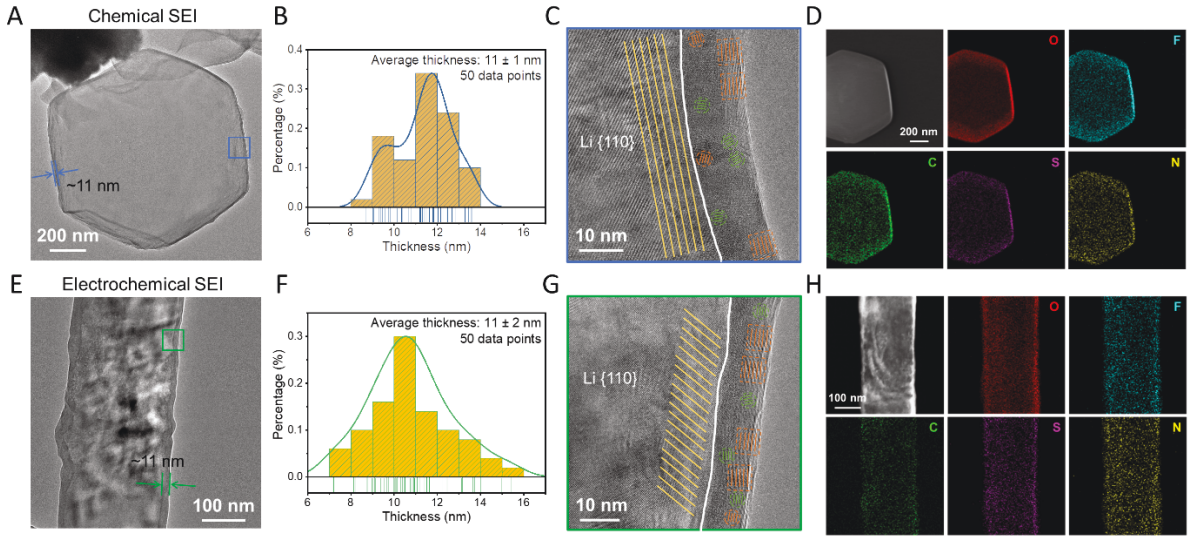

Fig. 4. Cryo-EM analysis on structure and chemistry of chemical and electrochemical SEI in 4M LiFSI in DME. A) Cryo-EM image of faceted Li particle covered with a layer of chemical SEI. B) Thickness statistics of chemical SEI. C) High-resolution cryo-EM image of chemical SEI layer, magnified from the blue box in (A). D) STEM EDS mapping of chemical SEI. E-H) Analogous images to (A-D) but collected on electrochemical SEI.

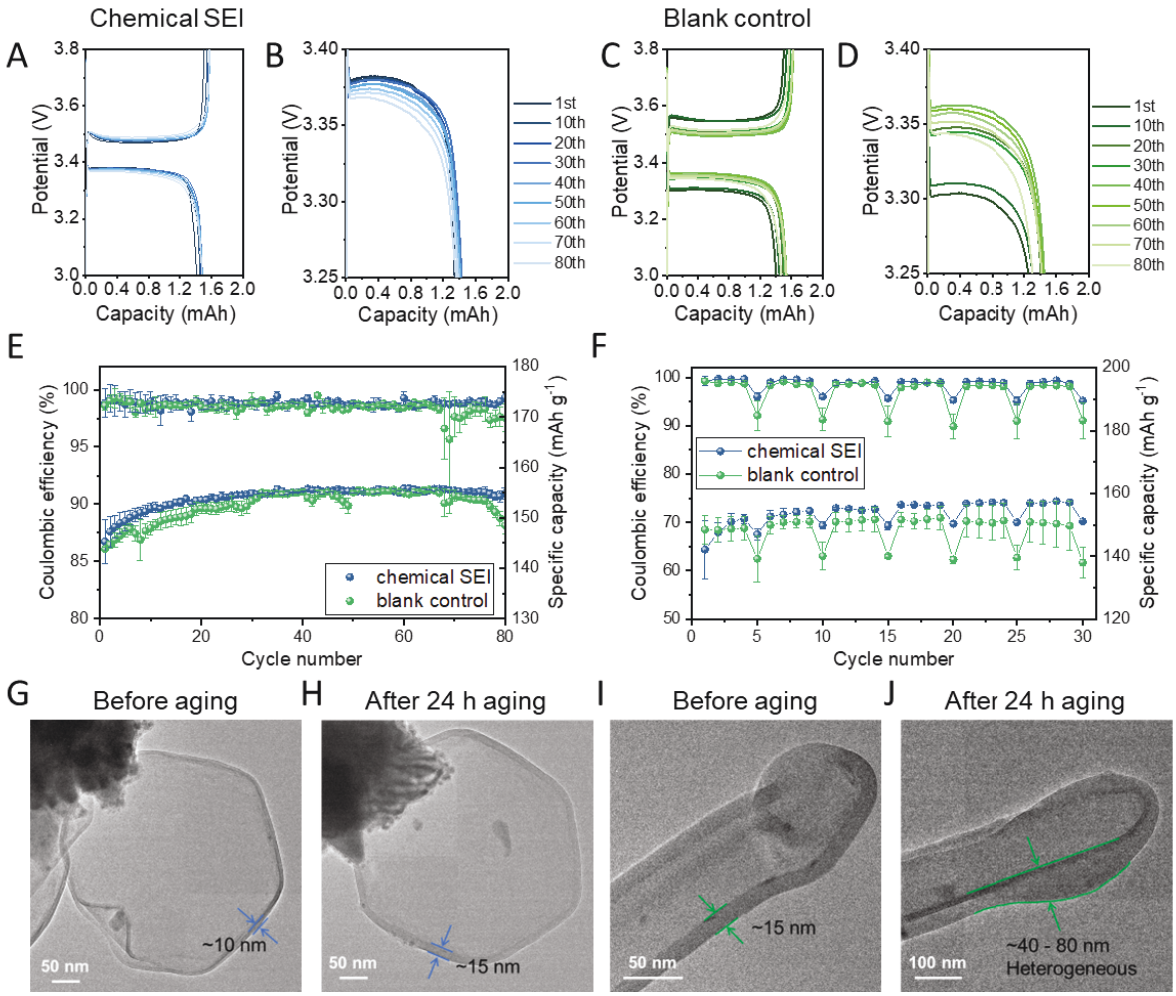

Fig 5. Effect of chemical SEI on electrochemical performance in Li||LFP cells in 1M $LiPF_6$ in EC/DEC. A) Representative voltage profiles of each ten cycles with zoomed-in view in (B). C) Representative voltage profiles of each ten cycles with calendar aging during every five cycles with zoomed-in view in (D). E) CE and specific capacity as a function of cycle number at 0.5 C. F) CE and specific capacity with calendar aging during every five cycles. Cryo-EM images of faceted Li particles in (G) and after 24-hour calendar aging in (H). Cryo-EM images of dendritic Li particles in (I) and after 24-hour calendar aging in (J).

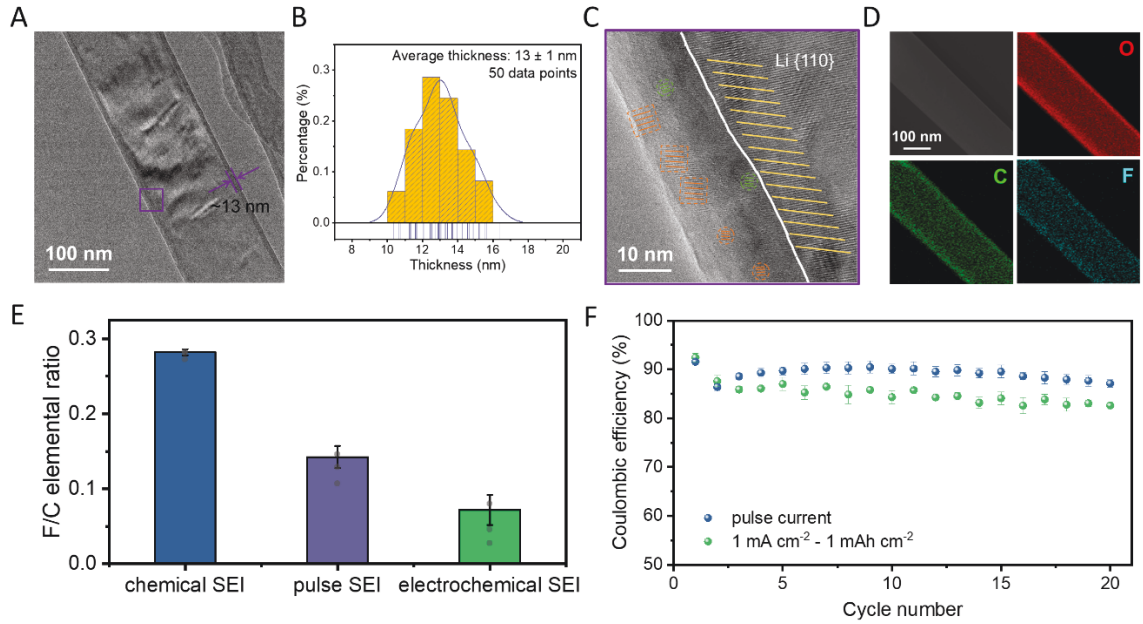

Fig 6. Structural and chemical analysis of pulse SEI in 1M $LiPF_6$ in EC/DEC. A) Cryo-EM image of Li dendrite covered with a layer of pulse SEI. B) Thickness statistics of pulse SEI. C) High-resolution cryo-EM image of pulse SEI layer, magnified from the purple box in (A). D) STEM EDS mapping of pulse SEI. E) F/C elemental ratio of pulse SEI compared to chemical and electrochemical SEI calculated from XPS analysis. F) CE comparison between pulse current protocol (at a current density of 1 mA cm^{-2}, with repeated deposition for 1 s and resting for 3 s, until a capacity of 1 mAh cm^{-2} is reached) and standard galvanostatic cycling protocol (at a current density of 1 mA cm^{-2}, until a capacity of 1 mAh cm^{-2} is reached).